PAPER

Perovskite-type hydrides ACaH₃ (A = Li, Na): computational investigation on materials properties for hydrogen storage applications†

Sol-Hyang Ri,‡[a] Un-Gi Jong, [iD] ‡*[b] Thae-Song Im[c] and Un-Ryong Rim [iD] *[d]

Recently, perovskite materials have emerged as a multifunctional material for photovoltaics, luminescence, photocatalytics and hydrogen storage applications. This work reports a theoretical investigation on materials properties of hydride perovskite ACaH₃ (A = Li, Na) with cubic phase of $Pm\bar{3}m$ space group for application of H₂ storage material. Electronic structure calculations show that the cubic LiCaH₃ and NaCaH₃ have an indirect bandgaps of 2.1 and 2.3 eV with valence band maximum at R point and conduction band minimum at M point. Based on geometric factors, elastic constants and self-consistent phonon calculations, we reveal that ACaH₃ can be dynamically stabilized in cubic phase at elevated temperatures, and the compounds are mechanically stable as well, satisfying Born's stability criteria. Finally, our calculations demonstrate that gravimetric (volumetric) H₂ storage capacities are 5.99 and 4.54 wt% (63.77 and 60.93 g L⁻¹), and dehydrogenation temperatures are 453.76 and 688.16 K with a consideration of quantum effect for A = Li and Na, respectively. This work highlights that cubic LiCaH₃ is regarded as a potential H₂ storage material due to its high H₂ storage capacity, stability and suitable dehydrogenation temperature.

1 Introduction

Using hydrogen as a primary fuel in the long term would effectively reduce the world's dependence on fossil fuel without releasing any pollutant as by-products.[1–3] In the quest for feasible hydrogen-fueled vehicles, one of the major challenges is to develop lightweight materials with high hydrogen densities (>5 wt%) which can absorb and release hydrogen in the range of 1–10 bar and 298–473 K.[4] The U.S. Department of Energy (DOE) aims at developing a hydrogen storage material with a gravimetric capacity of 5.5 wt% and a volumetric capacity of 40 g L⁻¹ by 2025 for a target driving range of 300 miles.[5] Considerable research efforts have been concentrated on metal hydrides such

[a]Faculty of Distance Education, Kim Chaek University of Technology, Pyongyang, PO Box 76, Democratic People's Republic of Korea

[b]Faculty of Materials Science, Computational Materials Design (CMD), Kim Il Sung University, Pyongyang, PO Box 76, Democratic People's Republic of Korea. E-mail: ug.jong@ryongnamsan.edu.kp

[c]Faculty of Metal Engineering, Kim Chaek University of Technology, Pyongyang, PO Box 76, Democratic People's Republic of Korea

[d]Institute of Ocean Engineering, Kim Chaek University of Technology, Pyongyang, PO Box 76, Democratic People's Republic of Korea. E-mail: lur8971@star-co.net.kp

as Mg(BH₄)₂,[6–9] NaAlH₄,[10–13] LiBH₄,[14–16] MgH₂ (ref. 17–19) and LiH₂ (ref. 20) due to their relatively high hydrogen storage capacities and inexpensive production cost. However, most of these hydrides unfortunately suffer from poor kinetics and irreversibility of hydrogen absorption and desorption cycling. For example, it was demonstrated that LiBH₄ (ref. 15) can be dehydrogenated and rehydrogenated above its melting point (∼550 K) because of its slow kinetics and unfavorable thermodynamics, and only when heating up to 770 K, most of the hydrogen stored in LiBH₄ can be released from it. Moreover, some of them are likely to release toxic gas (e.g., ammonia, diborane) during the dehydrogenation reaction.[21] Nevertheless, the complex metal hydrides containing alkali metals are expected to have great potential for enhancing kinetics and reversibility as well as inhibiting release of pollutant.

In recent years, perovskite-type hydrides ABH₃ where A and B are monovalent and divalent cations respectively have attracted great attention as a promising candidate for the future hydrogen storage materials.[22–29] It was found that these compounds exhibit high thermodynamic stability, sufficient space to accommodate a large amount of hydrogen, catalytic effect on the hydrogen reversibility and high hydrogen storage capacity.[30–33] Ikeda et al. first synthesized the perovskite-type hydride NaMgH₃ by mechanically milling the binary hydrides of NaH and MgH₂ at ambient temperature, explaining the formation ability of other hydride perovskite from Goldschmidt tolerance factors.[23–26] They observed reversible hydrogenation and dehydrogenation with a hydrogen capacity of 5.9 wt% and

rapid hydrogen motion at elevated temperature. On the other hand, Komiya et al. fabricated the perovskite-type hydrides $AMgH_3$ (A = Na, K, Rb) by using ball-milling, reporting that the hydrides are dehydrogenated at temperatures between 673 and 723 K according to several ways depending on the type of A cation.[33] Furthermore, it was revealed that the hydride perovskite $ZrCoH_3$ can reversibly absorb and desorb hydrogen, but it suffers from the hydrogen-induced disproportionation (HID) phenomena.[34] However, it was proved that the HID can be improved by partial substitution of Zr or Co cation with Ti cation.[35]

Trigger by the experimental studies,[23–26] extensive theoretical investigations have been carried out to provide an in-depth understanding of materials properties for hydrogen storage applications of the perovskite-type hydrides.[22,28,30–32,36,37] In 2007, Fornari et al.[31] reported a density functional study on the structural and lattice dynamics properties for the perovskite hydrides $AMgH_3$ (A = Na, K, Rb), revealing the compound's ionic bonding nature and dynamical stability. Based on density functional theory (DFT) calculations, Gencer et al.[38] investigated the electronic and mechanical properties of the hydride perovskites $LiNiH_3$, $NaNiH_3$ and $KNiH_3$ with hydrogen storage capacities of 4.4, 3.6 and 3.3 wt% respectively, illustrating their mechanical stability and metallic nature. Siddique et al.[39,40] carried out DFT studies on the dynamical and mechanical stabilities of the hydride perovskites $LiBH_3$ (B = Sc, Ti, V) and AVH_3 (A = Be, Mg, Ca, Sr) with hydrogen storage capacities higher than 4.0 wt%, confirming their stabilities. Recently, Xu et al.[36] reported the hydrogen storage capacities and structural, electronic, optical, mechanical, thermodynamic and dynamical properties for $XAlH_3$ (X = Na, K) hydride perovskites. They concluded that the compounds show mechanical, dynamical and thermodynamical stabilities with metal-like electronic properties by ionic chemical bonding. Despite enormous researches on the hydride perovskites, little attention has been drawn to perovskite-type hydride $ACaH_3$ (A = Li, Na) for application as a hydrogen storage material. The $LiCaH_3$ and $NaCaH_3$ have high hydrogen storage capacities of 6.0 and 4.5 wt%, respectively and contain nontoxic and earth-abundant elements. Thus, the hydride perovskites $ACaH_3$ (A = Li, Na) can be regarded as a potential candidate for high-performance, low-cost and nontoxic hydrogen storage materials. In this work, we present a comprehensive and systematic investigation of the structural, electronic and lattice dynamic properties and thermodynamic and mechanical stabilities of the hydride perovskites $ACaH_3$ for the application as the hydrogen storage material by using first-principles calculations.

2   Computational methods

Density functional theory (DFT) calculations were performed using the Vienna ab initio simulation package (VASP).[44,45] The projector augmented wave (PAW) potentials[46,47] were used to describe the interactions between ions and valence electrons. The valence electron configurations were given as $Li–2s^1$, $Na–3s^1$, $Ca–3p^6 4s^2$ and $H–1s^1$. Convergence test revealed that the

cutoff energy 800 eV for plane wave basis sets and k-point mesh $10 \times 10 \times 10$ provided a total energy accuracy of 1 meV per atom (see Fig. S1, ESI†). The variable-cell structural optimizations were performed until the atomic forces were less than 10^{-3} eV $Å^{-1}$ with the self-consistent convergence threshold of 10^{-8} eV. We utilized the Perdew–Burke–Ernerhof (PBE)[48] and PBE-revised functionals for solid (PBEsol)[49] within the generalized gradient approximation (GGA) and the Perdew–Wang (PW91)[50] functional within the local density approximation (LDA) in order to account for the exchange-correlation (XC) interaction among the valence electrons. We computed the atomic forces for the $2 \times 2 \times 2$ supercells, using the reduced cutoff energy of 600 eV and k-point mesh of $4 \times 4 \times 4$ with the same convergence thresholds.

As proposed by Ikeda,[23] we considered the H_2 decomposition reaction for the hydride perovskite $ACaH_3$ as follows:

$$ACaH_3 \rightarrow A + Ca + \frac{3}{2}H_2. \tag{1}$$
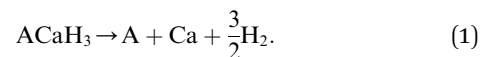
According to eqn (1), the H_2 decomposition enthalpy ΔH was calculated as follows:

$$\Delta H = H_A + H_{Ca} + \frac{3}{2}H_{H_2} - H_{ACaH_3} \tag{2}$$

where $H_{material}$ is an enthalpy for the corresponding material. Materials enthalpy H was computed as follows:

$$H = E_{\text{ele}} + E_{\text{zpe}} \tag{3}$$

where E_{ele} and E_{zpe} are the electronic total energy and the zero-point energy by quantum effect, respectively. Then, we estimated the E_{zpe} by using the following formula:

$$E_{\text{zpe}} = \frac{\int h\omega g(\omega)\mathrm{d}\omega}{2} \tag{4}$$

where h, ω and $g(\omega)$ are the Plank's quantum constant, phonon frequency and phonon density of state, respectively. The H_2 decomposition temperature T_{des} can be estimated as follows:

$$T_{\text{des}} = -\Delta H/\Delta S \tag{5}$$

where ΔH is the H_2 decomposition enthalpy and ΔS is the entropy increment in the decomposition reaction. In this work, we approximate the ΔS to the entropy of H_2 gas, 130.7 J mol^{-1} K^{-1}.[51]

Hydrogen storage materials are utilized to store and release hydrogen for the applications of the hydrogen-powered vehicles, fuel cells and energy storage medium. Thus, their mechanical stabilities are a crucial factor because they determine the hydrogen storage system's durability and safety under operation. In order to estimate the materials mechanical stability, we evaluated the elastic constants such as bulk (B), shear (G) and Young's (E) moduli, which represent linear response of lattice to small strain. The elastic stiffness (C_{ij}) and compliance (S_{ij}) constants were obtained from the density functional perturbation theory (DFPT)[52] calculations using the PBEsol functional.

Table 1 Structural parameters calculated using the PW91, PBE and PBEsol functionals and geometric factor t_G and t_o for the cubic $LiCaH_3$, $NaCaH_3$, Li, Na and Ca compounds with previous experimental data.[3]

Compound	Atom	PW91 Lattice constants (Å)	PW91 Position x	y	z	PBE Lattice constants (Å)	PBE Position x	y	z	PBEsol Lattice constants (Å)	PBEsol Position x	y	z	Exp. Lattice constants (Å)	Exp. Position x	y	z	Geometric factor t_G	t_o
$LiCaH_3$	Li	$a = 4.25$	0.5	0.5	0.5	$a = 4.29$	0.5	0.5	0.5	$a = 4.28$	0.5	0.5	0.5	—	—	—	—	0.8	0.7
	Ca		0.0	0.0	0.0		0.0	0.0	0.0		0.0	0.0	0.0	—	—	—	—		
	H1		0.5	0.0	0.0		0.5	0.0	0.0		0.5	0.0	0.0	—	—	—	—		
	H2		0.0	0.5	0.0		0.0	0.5	0.0		0.0	0.5	0.0	—	—	—	—		
	H3		0.0	0.0	0.5		0.0	0.0	0.5		0.0	0.0	0.5	—	—	—	—		
$NaCaH_3$	Na	$a = 4.31$	0.5	0.5	0.5	$a = 4.35$	0.5	0.5	0.5	$a = 4.34$	0.5	0.5	0.5	—	—	—	—	0.9	0.7
	Ca		0.0	0.0	0.0		0.0	0.0	0.0		0.0	0.0	0.0	—	—	—	—		
	H1		0.5	0.0	0.0		0.5	0.0	0.0		0.5	0.0	0.0	—	—	—	—		
	H2		0.0	0.5	0.0		0.0	0.5	0.0		0.0	0.5	0.0	—	—	—	—		
	H3		0.0	0.0	0.5		0.0	0.0	0.5		0.0	0.0	0.5	—	—	—	—		
Li	Li1	$a = 3.44$	0.5	0.5	0.5	$a = 3.49$	0.5	0.5	0.5	$a = 3.47$	0.5	0.5	0.5	$a = 3.47^a$	0.5	0.5	0.5		
	Li2		0.0	0.0	0.0		0.0	0.0	0.0		0.0	0.0	0.0		0.0	0.0	0.0		
Na	Na1	$a = 4.17$	0.5	0.5	0.5	$a = 4.25$	0.5	0.5	0.5	$a = 4.23$	0.5	0.5	0.5	$a = 4.22^b$	0.5	0.5	0.5		
	Na2		0.0	0.0	0.0		0.0	0.0	0.0		0.0	0.0	0.0		0.0	0.0	0.0		
Ca	Ca1	$a = 5.51$	0.0	0.0	0.0	$a = 5.61$	0.0	0.0	0.0	$a = 5.59$	0.0	0.0	0.0	$a = 5.57^c$	0.0	0.0	0.0		
	Ca2		0.5	0.5	0.0		0.5	0.5	0.0		0.5	0.5	0.0		0.5	0.5	0.0		
	Ca3		0.5	0.0	0.5		0.5	0.0	0.5		0.5	0.0	0.5		0.5	0.0	0.5		
	Ca4		0.0	0.5	0.5		0.0	0.5	0.5		0.0	0.5	0.5		0.0	0.5	0.5		

[a] Experiment.[41] [b] Experiment.[42] [c] Experiment.[43]

$$B_V = \frac{C_{11} + 2C_{12}}{3}, \quad G_V = \frac{C_{11} - C_{12} + 3C_{44}}{5}$$

$$B_R = \frac{1}{3(S_{11} + 2S_{12})}, \quad G_R = \frac{5}{4S_{11} - 4S_{12} + 3S_{44}} \quad (6)$$

$$B = \frac{B_V + B_R}{2}, \quad G = \frac{G_V + G_R}{2}, \quad E = \frac{9GB}{3B + G}$$

For the cubic phase, there exist three independent stiffness constants such as C_{11}, C_{12} and C_{44}. According to the Born's stability criteria,[53] the cubic crystalline solids are mechanically stable when satisfying the following eqn (7):

$$C_{11} > 0, \ C_{44} > 0, \ C_{11} + 2C_{12} > 0, \ C_{11} - C_{12} > 0 \quad (7)$$

In order to calculate the phonon density of state (DOS) and the E_{zpe}, we computed the phonon dispersion curves for all the compounds involved in the H_2 decomposition reaction eqn (1). The phonon dispersion curves and DOS calculations were carried out by using the finite displacement method, as implemented in the ALAMODE code.[54,55] Using $2 \times 2 \times 2$ supercells, we prepared 30 different configurations where all the atoms were randomly displaced by 0.01–0.06 Å from their equilibrium positions for the cubic $ACaH_3$, A and Ca compounds, respectively. We then calculated the atomic forces for all the displaced configurations by performing precise DFT calculations, and harmonic and anharmonic interatomic force constants (IFCs) were extracted by using the compressive sensing lattice dynamics (CSLD),[56] as implemented in the ALAMODE code. We ensure that for all the compounds, the IFCs can reproduce the atomic forces within the relative errors less than 2.4% when comparing to the DFT-calculated forces. The harmonic IFCs were extracted by considering all the possible harmonic terms, whereas the cubic and quartic anharmonic IFCs were extracted by setting the cutoff distance up to the 8th – and 5th – nearest neighbor for each type of atom. The self-consistent phonon (SCP) calculations[57] were carried out to obtain temperature-dependent phonon dispersion curves and DOS by considering the anharmonic effects at finite temperatures.

3 Results and discussion

3.1 Crystal structures

Perovskite-type compounds are generally regarded to successively crystallize in orthorhombic, tetragonal and cubic phases upon increasing temperature. In fact, it was experimentally found that $MMgH_3$ (M = Na, K, Rb) adopt the cubic and orthorhombic phases at different temperatures.[21,23,33] As for the perovskite compounds ABH_3, the stability of the perovskite structure can be empirically assessed by using the Goldschmidt tolerance factor $t_G = (r_A + r_B)/\sqrt{2}(r_B + r_H)$ and octahedral factor $t_o = r_B/r_H$, where r_A, r_B and r_H are the ionic radii for A^+, B^{2+} and H^- ions, respectively. The t_o can be used to assess whether the BH_6 octahedron is stable, while the t_G to check whether the A-site cation can fit between the BH_6 octahedra. According to the empirical criteria,[58,59] the perovskite compounds can adopt the stable cubic phase when satisfying $1.0 \geq t_G \geq 0.8$ and $t_o \geq$

0.4. This criteria have been successfully applied to estimate the formability of cubic phase for the oxide, halide and fluoride perovskites.[60,61] Table 1 lists the calculated geometric factors of t_G and t_o for the hydride perovskites $ACaH_3$ (A = Li, Na). Based on the analysis of geometric factors, it was found that the hydride perovskites $LiCaH_3$ and $NaCaH_3$ can stabilize in the cubic phase because of suitable geometric factors of $t_G = 0.8, 0.9$ and $t_o = 0.7$. Therefore, it was supposed that the hydride perovskites $ACaH_3$ can adopt the cubic phase with the $Pm\bar{3}m$ space group like the oxide, halide and fluoride perovskites (see Fig. 1). We note that even though the structural factors of t_G and t_o can provide a qualitative estimation of the perovskite structure stability, a quantitative and detailed assessment of materials stability should be based on precise calculations of lattice dynamics properties and elastic constants.

Through the variable-cell structural optimization by using the PW91, PBE and PBEsol functionals, we calculated the equilibrium lattice constants for the cubic $ACaH_3$, Ca, Li and Na compounds. According to the previous experiments,[41–43] we assume that the Ca and Li (Na) compounds adopt the cubic phases with the space group of $Fm\bar{3}m$ and $Im\bar{3}m$, respectively (see Fig. S2, ESI†). The calculated lattice constants are listed in Table 1. The PBEsol-calculated lattice constant of $LiCaH_3$ is $a = 4.28$ Å, which is slightly smaller than $a = 4.34$ Å of $NaCaH_3$ because of the smaller ionic radius of Li cation than Na cation. To the best of our knowledge, there are no experimental and theoretical works of the hydride perovskites $ACaH_3$ for comparison. However, the optimized lattice constants are in good agreement with the previous experiments[41–43] for the cubic Ca, Li and Na. Especially, the PW91-calculated lattice constants of $a = 5.51, 4.17$ and 3.44 Å underestimate the experimental ones[41–43] of $a = 5.59, 4.23$ and 3.47 Å for the cubic Ca, Na and Li respectively, whereas the PBE-calculated ones slightly
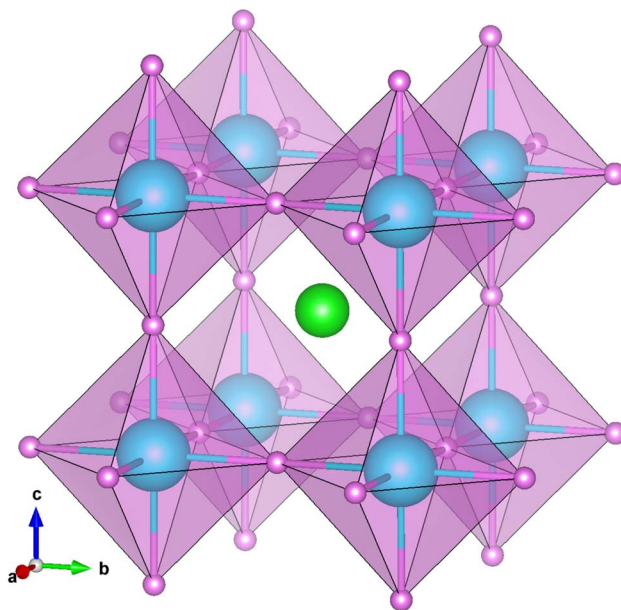

Fig. 1 Polyhedral view of crystalline structure optimized using PBEsol functional for cubic $ACaH_3$ with a space group of $Pm\bar{3}m$. The green, cyan and purple balls represent the A, Ca and H atoms, respectively.

overestimate the experimental ones. Moreover, the PBEsol-calculated lattice constants of $a = 5.59$, 4.23 and 3.47 Å are in excellent agreement with the experimental ones of $a = 5.59$, 4.23 and 3.47 Å, providing a relative error less than 0.5%. Hereby, we adopted the PBEsol functional for the calculations of lattice dynamics and electronic structure properties, mechanical stability and H_2 decomposition energetics for the cubic $ACaH_3$.

3.2 Lattice dynamics properties

In order to predict lattice dynamics properties, we calculated the phonon dispersion curves and density of states (DOS) at elevated temperatures for the cubic $ACaH_3$ (A = Li, Na) with a space group of $Pm\bar{3}m$ by using the SCP theory. From the phonon dispersions and DOS (Fig. 2), we can directly estimate the material's dynamical stability and compute the zero-point E_{zpe} energy in consideration of quantum effect by using eqn (4). As calculated at 0 K, Fig. 2 shows the harmonic phonon dispersion curves (blue-colored lines in the left panel) computed along the high symmetry line of Γ–X–M–Γ–R in the phonon Brillouin zone (BZ). It was found that the relatively deep negative phonon eigenvalues reaching up to −70 meV, known as the soft mode, appear in the whole phonon BZ range for the cubic $ACaH_3$. Such finding indicates that these compounds are dynamically unstable in the cubic phase at 0 K. From the phonon DOS at 0 K (middle panel in Fig. 2), we found that these soft phonon modes are mainly ascribed to the Ca- and Li-atomic (Na- and H-atomic) vibrations for the $LiCaH_3$ ($NaCaH_3$).The symmetry analysis of the phonon eigenvectors indicates that the soft phonon modes are responsible for symmetry breaking instabilities like in the halide and oxide perovskites.[62,63] As shown in Fig. 3(a), the lowest soft mode at the Γ point induces the displacement of Li and Ca atoms from the ideal centers of the CaH_3 inorganic framework and the CaH_6 octahedron,
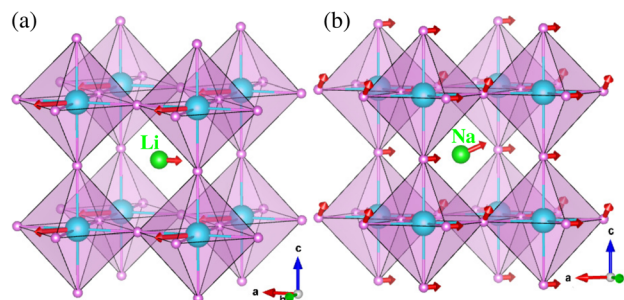

Fig. 3 Polyhedral view of strong anharmonic vibrations at 0 K associated with the lowest soft phonon modes at the Γ point for the cubic (a) $LiCaH_3$ and (b) $NaCaH_3$. The red arrows display the atomic displacement vectors. The green, cyan and purple balls represent the Li (Na), Ca and H atoms, respectively.

respectively for the cubic $LiCaH_3$. Moreover, the lowest soft modes causes collective displacements of the H and Na atoms with a larger magnitude of Na displacement for the cubic $NaCaH_3$ (Fig. 3(b)). The presence of such soft modes suggests that the cubic hydride perovskites $ACaH_3$ can undergo a phase transition to a lower symmetry structure such as tetragonal or orthorhombic phase upon decreasing temperature like the halide and oxide perovskites. The calculated phonon dispersion curves and DOS are plotted in Fig. S3–S5, ESI† for the cubic Li, Na and Ca without any soft phonon modes, implying their dynamical stabilities.

To clearly estimate the phase stability, we renormalized the phonon dispersion curves and DOS at elevated temperatures from 300 to 900 K with an interval of 200 K by using the SCP theory. From the SCP calculations, the negative phonon energies corresponding to the soft modes were renormalized to be real within the whole range of the phonon BZ (orange and red
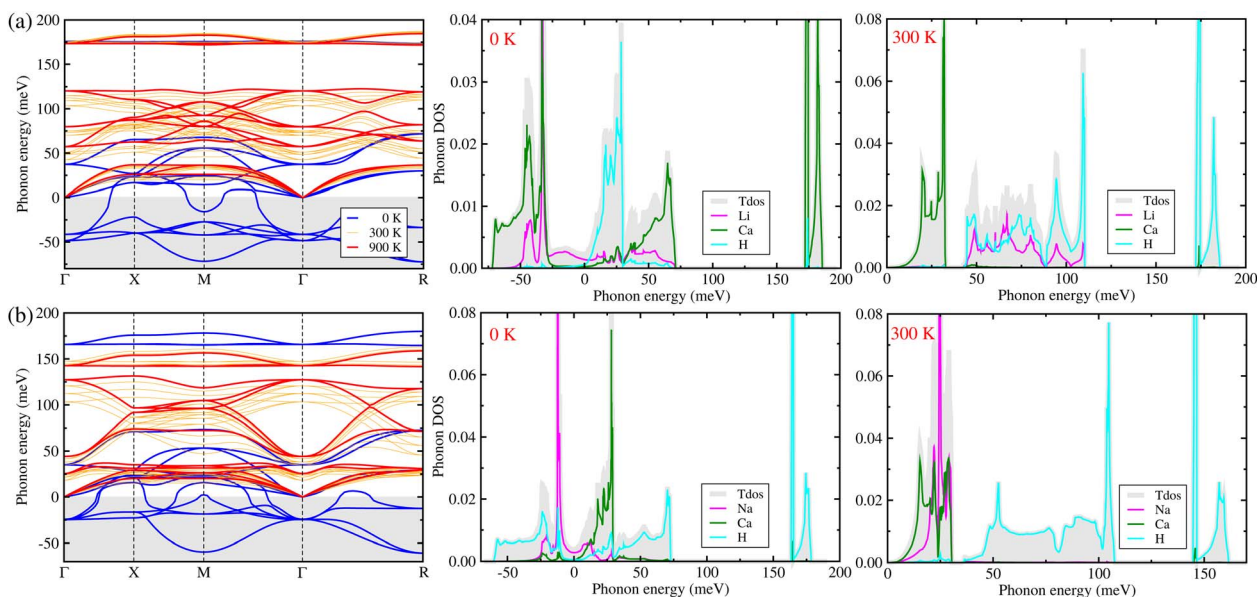

Fig. 2 Phonon dispersion curves and atom-projected phonon density of states (DOS) calculated by using the self-consistent phonon (SCP) theory at elevated temperatures for the hydride perovskites (a) $LiCaH_3$ and (b) $NaCaH_3$ with the cubic phase of a space group of $Pm\bar{3}m$. The thick blue and red lines display the phonon dispersion curves calculated at 0 and 900 K, respectively, while the thin orange lines at 300, 500 and 700 K.

lines in the left panel of Fig. 2), which indicates that the cubic phase of ACaH$_3$ is dynamically stable at elevated temperatures, as confirmed in experiment[33] for the Mg-based hydride perovskites AMgH$_3$ (A = Na, K, Rb). In particular, the negative phonon energies of −49 and −38 (−26) meV were renormalized at 900 K to 81 and 129 (40 and 125) meV at the Γ point for LiCaH$_3$ (NaCaH$_3$). Noticeable changes were observed for the phonon DOS as well (right panel in Fig. 2). For instance, at 300 K, the H and Ca atoms in both LiCaH$_3$ and NaCaH$_3$ play dominant roles in the high-lying optical phonon modes and the acoustic phonon modes coupled with the low-lying optical modes, respectively. However, in the case of LiCaH$_3$, the Li atom makes a dominant contribution to the mid-lying phonon modes ranging from 40 to 115 meV, while in the case of NaCaH$_3$, the Na atom significantly contributes to the acoustic and low-lying optical modes below 30 meV. Upon increasing temperature, the phonon dispersion curves and phonon DOS broaden towards higher energy due to stronger atomic vibrations (see Fig. S6 and S7, ESI†).

3.3 Electronic structure properties

Considering that the cubic phase can be stabilized at elevated temperatures, we calculated the electronic structure properties for the cubic hydride perovskite ACaH$_3$ with the space group of $Pm\bar{3}m$ by using the PBEsol functional. Using the calculated energy band structures (Fig. 4(a)), we can directly estimate the energy band gap, and from the atom-projected electron DOS (Fig. 4(b)), we can understand which atom can play important role near the Fermi level E_f. It was established that the PBE or PBEsol functional within the GGA can describe electronic structure properties in good agreement with experiment for the halide and hydride perovskites. The spin–orbit coupling (SOC) effect was not considered as all the constituent atoms are very light for ACaH$_3$. Fig. 4(a) shows the energy band structure calculated along the high symmetry line of R–Γ–X–R–X_1–M–Γ–X_1 in the BZ for the cubic LiCaH$_3$. It was found that the compound has an indirect band gap of 2.1 eV with the valence band maximum (VBM) at the R point and the conduction band minimum (CBM) at the M point, and a direct band gap of 2.8 eV at the R point. Meanwhile, the cubic NaCaH$_3$ provides an indirect (direct) band gap of 2.3 (3.2) eV with similar band structures to the LiCaH$_3$ (see Fig. S8, ESI†). It is worth noting that the larger the ionic radii of A cation, the larger band gaps the hydride perovskites ACaH$_3$ provide, being similar to the case of the halide and fluoride perovskites.[60,61] Through the analysis of atom-projected partial DOS, it was revealed that the valence bands (VBs) are dominated by H-s state with a small contribution of Ca-s states, while the conduction bands (CBs) are dominated by Ca-s states coupled with Li- and H-s states (see Fig. 4 and S8, ESI†). Such analysis coincides with the isosurface plot of the electron charge density corresponding to the VBM and CBM, as shown in Fig. 5.

3.4 Mechanical stability and H$_2$ decomposition energetics

In order to assess the mechanical stability of the compounds, we then estimated the elastic constants such as the stiffness
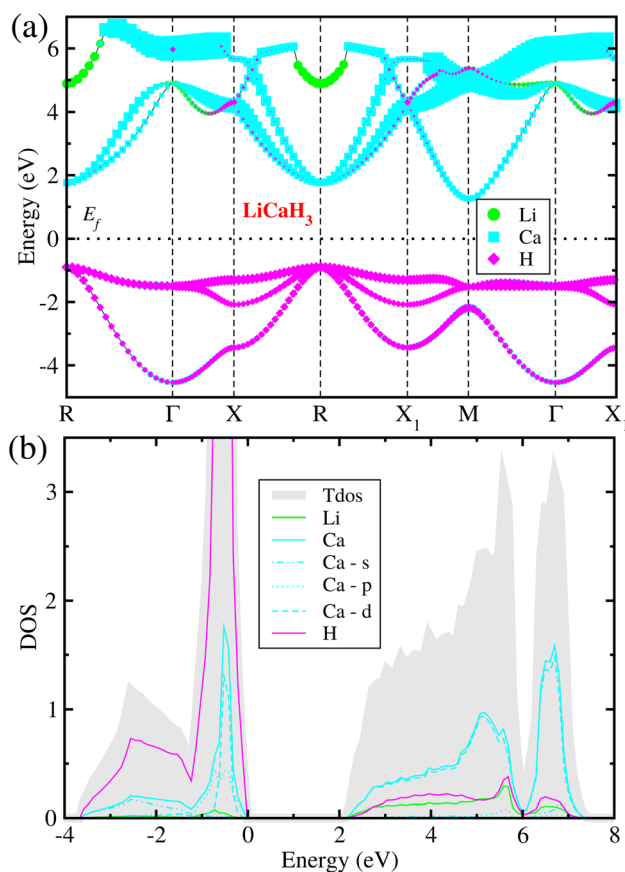

Fig. 4 (a) Atom-resolved electronic band structure and (b) partial density of states (DOS) calculated with the PBEsol functional for the hydride perovskite LiCaH$_3$ in the cubic phase.
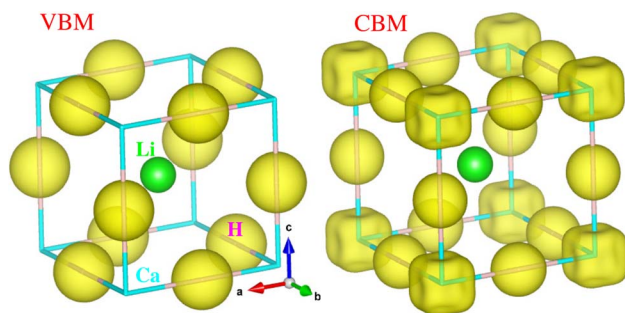

Fig. 5 Isosurface plot of charge density corresponding to the conduction band minimum (CBM) and valence band maximum (VBM) at the values of 0.02 |e| Å^{-3} in the cubic ACaH$_3$. The green, cyan and purple balls represent the Li (Na), Ca and H atoms, respectively.

constant (C_{ij}), bulk modulus (B), shear modulus (G) and Young's modulus (E) by using the DFPT calculations. As listed in Table 2, the elastic stiffness constants of C_{11}, C_{12} and C_{44} satisfy the Born's stability criteria for the cubic LiCaH$_3$ and NaCaH$_3$, expressed as eqn (7). Furthermore, we found that the cubic LiCaH$_3$ (NaCaH$_3$) is a ductile (brittle) material according to the Pugh's criteria[64] because the Poisson's ratio ν and the Pugh's ratio B/G are larger (smaller) than the threshold values of 0.26

Table 2 Gravimetric and volumetric H_2 storage density (ρ_g and ρ_v), elastic stiffness constant (C_{ij}), bulk modulus (B), shear modulus (G), Young's modulus (E), Pugh's ratio (B/G), Poisson's ratio (ν), zero-point energy (E_{zpe}), H_2 decomposition enthalpy (ΔH) and decomposition temperatures (T_{des} and T_{des}^q without and with quantum effect) for the cubic $ACaH_3$

Functional	Properties	LiCaH$_3$	NaCaH$_3$	Li	Na	Ca	H$_2$
	ρ_g (wt%)	5.99	4.54				
	ρ_v (g L^{-1})	63.77	60.93				
PW91	H (eV)	−14.92	−14.85	−3.77	−2.61	−7.73	−6.81
	ΔH (eV)	0.89	1.39				
	T_{des} (K)	437.42	687.23				
PBE	H (eV)	−14.73	−14.64	−3.81	−2.62	−7.73	−6.77
	ΔH (eV)	0.73	1.24				
	T_{des} (K)	361.68	612.46				
PBEsol	H (eV)	−14.74	−14.66	−3.92	−2.80	−8.54	−6.51
	ΔH (eV)	0.87	1.35				
	T_{des} (K)	430.86	666.23				
	E_{zpe} (eV)	0.37	0.37	0.34	0.02	0.01	0.27
	T_{des}^q (K)	453.76	688.16				
	C_{11} (GPa)	661.99	631.11				
	C_{12} (GPa)	83.89	95.43				
	C_{44} (GPa)	90.46	122.79				
	B (GPa)	276.59	273.99				
	G (GPa)	147.32	168.78				
	E (GPa)	375.33	420.09				
	B/G	1.87	1.62				
	ν	0.27	0.24				

and 1.75, respectively (see Table 2). Based on such analysis, it was found that the cubic $ACaH_3$ is mechanically as well as dynamically stable. Due to the larger B (smaller G and E), the LiCaH$_3$ exhibits greater (smaller) hardness upon bulk (shear and tensile) deformation compared to the NaCaH$_3$. On the other hand, both LiCaH$_3$ and NaCaH$_3$ are elastically anisotropic in nature because the anisotropic factor $A = 2C_{44}/(C_{11} - C_{12})$ is much smaller than unity.

Finally, we investigated the H_2 storage capacities and decomposition energetics for the hydride perovskites $ACaH_3$ (A = Li, Na). The H_2 gravimetric and volumetric storage capacities were calculated by using the formula of $\rho_g = 3M_H/(M_A + M_{Ca} + 3M_H) \times 100\%$ and $\rho_v = 3M_H/(N_A V_o)$, where M_A, M_{Ca} and M_H are the molar masses of A, Ca and H atoms, respectively while N_A and V_o are the Avogadro number and PBEsol-optimized unit cell volume. As shown in Table 2, the LiCaH$_3$ and NaCaH$_3$ have ρ_g (ρ_v) of 5.99 and 4.54 wt% (63.77 and 60.93 g L^{-1}), respectively, being larger or comparable to the targeted values of 5.5 wt% (40 g L^{-1}) provided by the U.S. DOE.

The H_2 decomposition temperature T_{des}^q (T_{des}) with (without) a consideration of the quantum effect was estimated by employing the eqn (5). Ignoring the quantum effect, the PBEsol-calculated T_{des} is 430.86 and 666.23 K for the cubic LiCaH$_3$ and NaCaH$_3$, respectively. With the calculated phonon energies and DOS, we calculated the zero-point energy E_{zpe}, finding that by considering the quantum effect, the T_{des}^q was slightly increased to 453.76 and 688.16 K for LiCaH$_3$ and NaCaH$_3$, respectively. To sum up, the hydride perovskite LiCaH$_3$ can store 5.99 wt% and 63.77 g L^{-1} hydrogen with mechanical and dynamical stabilities and suitable H_2 decomposition temperature of about 450 K, satisfying the U.S. DOE requirement.

4   Conclusions

In conclusion, by using the first-principles calculations, we have theoretically investigated the materials properties such as structural, electronic and lattice dynamics properties and mechanical and dynamical stabilities of the hydride perovskites $ACaH_3$ (A = Li, Na) in cubic phase of $Pm\bar{3}m$ space group for the application of hydrogen storage material. From the calculations of Goldschmidt tolerance factor t_G and octahedral factor t_o, it was suggested that the $ACaH_3$ (A = Li, Na) can stabilize in the cubic phase of $Pm\bar{3}m$ space group. We found that the PBEsol-calculated lattice constants and atomic positions are in good accordance with the available experimental data, while the PBE(PW91) functional slightly overestimate (underestimate) the structural properties for Li, Na and Ca metals. From the electronic structure calculations, it was found that the cubic LiCaH$_3$ and NaCaH$_3$ have an indirect (direct) bandgaps of 2.1 and 2.3 (2.8 and 3.2) eV with the VBM at the R point and the CBM at the M point (at the R point). The electron partial DOS indicated that the H-s and Ca-s states make significant contributions to the valence and conduction bands, respectively. The harmonic phonon dispersions and DOS calculations revealed that the cubic phase is dynamically unstable at 0 K with the negative phonon energies in the whole range of phonon BZ. However, the negative phonon energies were renormalized to be real by the SCP calculations, indicating that the $ACaH_3$ can be dynamically stabilized in the cubic phase at elevated temperatures. Based on the DFPT calculations of elastic constants, it was demonstrated that the cubic phase of $ACaH_3$ is mechanically stable in accordance with the Born's stability criteria. Finally, we investigated the H_2 storage capacities and decomposition temperature by considering the quantum effect,

finding that ρ_g (ρ_v) is 5.99 and 4.54 wt% (63.77 and 60.93 g L^{-1}), and T_{des}^q is 453.76 and 688.16 K for A = Li and Na, respectively. Based on such calculations, it was concluded that the hydride perovskite LiCaH$_3$ is a potential candidate for the onboard hydrogen storage application with the high gravimetric and volumetric capacities of 5.99 wt% and 63.77 g L^{-1} and a suitable dehydrogenation temperature of 453.76 K.

Data availability

The data supporting this article have been included as part of the ESI.†

Author contributions

Sol-Hyang Ri and Un-Gi Jong developed the original project, performed the DFT calculations and drafted the first manuscript. Un-Gi Jong and Un-Ryong Rim supervised the work. All authors reviewed the manuscript.

Conflicts of interest

There are no conflicts to declare.

Acknowledgements

References

1 L. W. Jones, *Science*, 1971, **174**, 367–370.
2 J. O. Bockris and M. A, *Science*, 1972, **176**, 1323.
3 G. W. Crabtree, M. S. Dresselhaus and M. V. Buchanan, *Phys. Today*, 2004, **57**, 39–44.
4 L. E. Klebanoff and J. O. Keller, *Int. J. Hydrogen Energy*, 2013, **38**, 4533–4576.
5 https://www.energy.gov/eere/fuelcells/doe-technical-targetsonboard-hydrogen-storage-light-duty-vehicles, 2022.
6 E. I. Epelle, K. S. Desongu, W. Obande, A. A. Adeleke, P. P. Ikubanni, J. A. Okolie and B. Gunes, *Int. J. Hydrogen Energy*, 2022, **47**, 20398–20431.
7 J. Andersson and S. Gronkvist, *Int. J. Hydrogen Energy*, 2019, **44**, 11901–11919.
8 J. Liu, L. Sun, J. Yang, D. Guo, D. Chen, L. Yang and P. Xiao, *RSC Adv.*, 2022, **12**, 35744–35755.
9 X. Hu, J. Wang, S. Li, X. Hu, R. Ye, L. Zhou, P. Li and C. Chen, *RSC Adv.*, 2023, **13**, 14980–14990.
10 Y. Liu, X. Zhang, K. Wang, Y. Yang, M. Gao and H. Pan, *J. Mater. Chem.*, 2016, **4**, 1087–1095.
11 E. Arora, S. Saini, P. Basera, M. Kumar, A. Singh and S. Bhattacharya, *J. Phys. Chem. C*, 2019, **123**, 62–69.
12 S. Zheng, F. Fang, G. Zhou, G. Chen, L. Ouyang, M. Zhu and D. Sun, *Chem. Mater.*, 2008, **20**, 3954–3958.
13 C. Milanese, S. Garroni, F. Gennari, A. Marini, T. Klassen, M. Dornheim and C. Pistidda, *Metals*, 2018, **8**, 567–578.
14 Y. Luo, L. Sun, F. Xu and Z. Liu, *J. Mater. Chem. A*, 2018, **6**, 7293–7309.
15 G. Xu, W. Zhang, Y. Zhang, X. Zhao, P. Wen and D. Ma, *RSC Adv.*, 2018, **8**, 19353–19361.
16 M. V. Sofianos, D. A. Sheppard, M. R. Rowles, T. D. Humphries, S. Liu and C. E. Buckley, *RSC Adv.*, 2017, **7**, 36340–36350.
17 M. Dornheim, S. Doppiu, G. Barkhordarian, U. Boesenberg, T. Klassen, O. Gutfleisch and R. Bormann, *Scr. Mater.*, 2007, **56**, 841–846.
18 S. Rivoirard, P. de Rango, D. Fruchart, J. Charbonnier and D. Vempaire, *J. Alloys Compd.*, 2003, **356**, 622–628.
19 C. Pohlmann, L. Rontzsch, J. Hu, T. Weigarber, B. Kieback and M. Fichtner, *J. Power Sources*, 2012, **205**, 173–179.
20 Y. Nakamori and S. i. Orimo, *Appl. Phys. Lett.*, 2006, **88**, 112104–112106.
21 H. Wu, W. Zhou, T. J. Udovic, J. J. Rush and T. Yildirim, *Chem. Mater.*, 2008, **20**, 2335–2342.
22 M. M. Parvaiz, A. Khalil, M. B. Tahir, S. Ayub, T. E. Alic and H. T. Masoodd, *RSC Adv.*, 2024, **14**, 8385–8396.
23 K. Ikeda, Y. Kogure, Y. Nakamori and S. Orimo, *Scr. Mater.*, 2005, **53**, 319–322.
24 K. Ikeda, S. Kato, Y. Shinzato, N. Okuda, Y. Nakamori, A. Kitano, H. Yukawa, M. Morinaga and S. Orimo, *J. Alloys Compd.*, 2007, **446**, 162–165.
25 K. Ikeda, Y. Kogure, Y. Nakamori and S. Orimo, *Prog. Solid State Chem.*, 2007, **35**, 329–337.
26 K. Ikeda, Y. Nakamori and S. Orimo, *Acta Mater.*, 2005, **53**, 3453–3457.
27 H. Wang, J. Zhang, J. W. Liu, L. Z. Ouyang and M. Zhu, *J. Alloys Compd.*, 2013, **580**, 197–201.
28 C. Kurkcu, S. Al and C. Yamcicier, *Eur. Phys. J. B*, 2022, **595**, 180–190.
29 T. Sato, D. Noreus, H. Takeshita and U. Haussermann, *J. Solid State Chem.*, 2005, **178**, 3381–3388.
30 W. Azeem, S. Hussain, F. A. Muhammad Khuram Shahzad, G. Khan, V. Tirth, H. Alqahtani, A. Algahtani, T. Al-Mughanam and Y. H. Wong, *Int. J. Hydrogen Energy*, 2024, **79**, 514–524.
31 M. Fornari, A. Subedi and D. J. Singh, *Phys. Rev. B: Condens. Matter Mater. Phys.*, 2007, **76**, 214118–214124.
32 M. K. Masood, W. Khan, K. Chaoui, Z. Ashraf, S. Bibi, A. Kanwal, A. A. Alothman and J. Rehman, *Int. J. Hydrogen Energy*, 2024, **63**, 1248–1257.
33 K. Komiya, N. Morisaku, R. Rong, Y. Takahashi, Y. Shinzato and H. Yukawa, *J. Alloys Compd.*, 2008, **453**, 157–160.
34 H. Q. Kou, H. He, W. H. Luo, T. Tang, Z. Y. Huang and G. Sang, *Int. J. Hydrogen Energy*, 2018, **43**, 322–328.
35 G. H. Zhang, G. Sang, R. J. Xiong, H. Q. Kou, K. Z. Liu and W. H. Luo, *Int. J. Hydrogen Energy*, 2015, **40**, 6582–6593.
36 N. Xu, R. Song, J. Zhang, Y. Chen, S. Chen, S. Li, Z. Jiang and W. Zhang, *Int. J. Hydrogen Energy*, 2024, **60**, 434–440.

37 M. López, M. B. Torres and I. Cabria, *Int. J. Hydrogen Energy*, 2024, **71**, 1363–1372.

38 A. Gencer and G. Surucu, *Int. J. Hydrogen Energy*, 2019, **44**, 15173–15182.

39 A. Siddique, A. Khalil, B. S. Almutairi, M. B. Tahir, T. Ahsan, A. Hannan, et al., *Chem. Phys.*, 2023, **568**, 111851–111859.

40 A. Siddique, A. Khalil, B. S. Almutairi, M. B. Tahir, M. Sagir, Z. Ullah, et al., *Int. J. Hydrogen Energy*, 2023, **48**, 24401–24411.

41 A. P. Frolov and K. P. Rodionov, *Science*, 1983, **219**, 1071–1072.

42 R. Berliner, O. Fajen, H. G. Smith and R. L. Hitterman, *Phys. Rev. B: Condens. Matter Mater. Phys.*, 1989, **40**, 12086–12097.

43 A. W. Hull, *Science*, 1920, **52**, 227.

44 G. Kresse and J. Furthmüller, *Comput. Mater. Sci.*, 1996, **6**, 15–50.

45 G. Kresse and J. Furthmüller, *Phys. Rev. B: Condens. Matter Mater. Phys.*, 1996, **54**, 11169–11186.

46 G. Kresse and D. Joubert, *Phys. Rev. B: Condens. Matter Mater. Phys.*, 1999, **59**, 1758–1775.

47 P. E. Blöchl, *Phys. Rev. B: Condens. Matter Mater. Phys.*, 1994, **50**, 17953–17979.

48 J. P. Perdew, K. Burke and M. Ernzerhof, *Phys. Rev. Lett.*, 1996, **77**, 3865–3868.

49 J. P. Perdew, A. Ruzsinszky, G. I. Csonka, O. A. Vydrov, G. E. Scuseria, L. A. Constantin, X. Zhou and K. Burke, *Phys. Rev. Lett.*, 2008, **100**, 136406–136411.

50 J. P. Perdew and Y. Wang, *Phys. Rev. B: Condens. Matter Mater. Phys.*, 1992, **45**, 13244–13252.

51 S. V. Alapati, J. K. Johnson and D. S. Sholl, *J. Phys. Chem. B*, 2006, **110**, 8769–8776.

52 S. Sharma, J. K. Dewhurst and C. Ambrosch-Draxl, *Phys. Rev. B: Condens. Matter Mater. Phys.*, 2003, **67**, 165332–165341.

53 B. Max and H. Kun, *Dynamical theory of crystal lattices*, Clarendon, Oxford, UK, 1956.

54 T. Tadano, Y. Gohda and S. Tsuneyuki, *J. Phys.: Condens. Matter*, 2014, **26**, 225402–225413.

55 T. Tadano and S. Tsuneyuki, *Phys. Rev. B: Condens. Matter Mater. Phys.*, 2015, **92**, 054301–054311.

56 Y. Xia, J. M. Hodges, M. G. Kanatzidis and M. K. Y. Chan, *Appl. Phys. Lett.*, 2018, **112**, 181906–181910.

57 M. Simoncelli, N. Marzari and F. Mauri, *Nat. Phys.*, 2019, **15**, 809–816.

58 W. Travis, E. N. K. Glover, H. Bronstein, D. O. Scanlon and R. G. Palgrave, *Chem. Sci.*, 2016, **7**, 4548–4556.

59 Z. Li, M. Yang, J. Park, S. Wei, J. J. Berry and K. Zhu, *Chem. Mater.*, 2016, **28**, 284–292.

60 U.-G. Jong, C.-J. Yu and Y.-H. Kye, *RSC Adv.*, 2020, **10**, 201–209.

61 C.-J. Pak, U.-G. Jong, C.-J. Kang, Y.-S. Kim, Y.-H. Kye and C.-J. Yu, *Mater. Adv.*, 2023, **4**, 4528–4536.

62 U.-G. Jong, C.-J. Yu, Y.-H. Kye, S.-N. Hong and H.-G. Kim, *Phys. Rev. Mater.*, 2020, **4**, 075403–075408.

63 U.-G. Jong, Y.-S. Kim, C.-H. Ri, Y.-H. Kye and C.-J. Yu, *J. Phys. Chem. C*, 2021, **125**, 6013–6019.

64 S. F. Pugh, *Philos. Mag.*, 1954, **45**, 823–843.